ACS APPLIED MATERIALS & INTERFACES

www.acsami.org

Research Article

Probing Strain-Induced Effects on Performance of Low-Dimensional Hybrid Perovskites for Solar Energy Harvesting

Robert Stanton, Sanjeev K. Gupta, and Dhara J. Trivedi*

Cite This: *ACS Appl. Mater. Interfaces* 2022, 14, 34603−34611

Read Online

ACCESS | Metrics & More | Article Recommendations | Supporting Information

ABSTRACT: The application of strain to photovoltaics (PVs), thermoelectrics (TEs), and semiconductors often has substantial impacts on the fundamental properties governing the efficiency of these materials. In this work, we investigate two stable phases of hybrid organic−inorganic two-dimensional (2D) perovskites (2DPKs) and their response to the application of tensile and compressive strain of up to 5%. These 2D $MAPbI_3$ analogues are known to exhibit strongly anisotropic properties and have been put forward as excellent candidates for application in mixed PV−TE devices. Our results, stemming from *ab initio* density functional theory calculations and investigation of transport properties through the Boltzmann transport equations, further elucidate the key properties contributing to the success of these materials. In particular, both the M1 and M2 phases exhibit stable structures between −5 and 5% biaxial strains. The M2 phase exhibits an excellent 23.8% power conversion efficiency under the application of 5% tensile strain. Furthermore, we analyze the effects of spin-orbit coupling on the band structures of both phases, revealing great potential for spintronic applications with the M2 phase, demonstrating Rashba coefficients up to 3.67 eV Å.

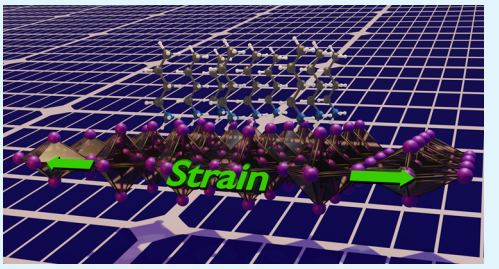

KEYWORDS: *two-dimensional perovskites, Rashba spin-orbit coupling, organic−inorganic hybrid perovskite, solar cell, thermoelectric*

INTRODUCTION

Hybrid organic−inorganic perovskites are a class of materials whose power conversion efficiency (PCE) in solar cell applications has dramatically increased from 3.8% in 2009 to 25.7% in 2020.[1−3] These improvements have spurred intensive research to break the 30% PCE barrier, approach the Shockley−Queisser limit, increase the stability and longevity of the perovskites, reduce usage of environmentally problematic compounds, and relevant to this study, expand control over the materials at the level of electronic structure.[4−11] Two-dimensional (2D) materials are unmatched in their ability to realize finely tunable optoelectronic properties through simple changes such as pressure modification, modulation in the number of layers, and exchange of interfacing materials.[12−16] This flexibility has led to successful application of 2D perovskites (2DPKs) as efficient light emitters, photodetectors, and hybrid photovoltaic (PV) and thermoelectric (TE) materials.[17−19] The 2D analogues of standard ABX_3 bulk hybrid perovskites (where A is an organic cation, B is Pb, Sn, or Ge, and X is a halogen anion) take the form of $A'_2A_{n-1}B_nX_{3n+1}$.[20] In hybrid 2DPKs, A′ is an organic cation generally of longer length than A, which acts as a spacer between the 2D or quasi-2D perovskite layers, n is the number of layers, and the identity of A, B, and X remains the same.

The reduction of dimensionality benefits not only the tunability of the materials but also their resilience to structural decomposition.[21,22] Structural stability has been a long-standing challenge for three-dimensional (3D) perovskites, as environmentally problematic lead-based materials are frequently used.[23] Although increased stability of 2DPKs tends to reduce efficiency in PV applications, previous work on 2DPKs for PV and TE applications has demonstrated that performance losses can be recovered through increased understanding and exploitation of layer dependence, dopant and defect concentration, and band engineering that is possible in these materials.[24−27] The latter is of particular interest in the current investigation because 2DPKs have emerged as excellent candidates for band modulation and spintronic applications owing to the existence of significant band splitting attributed to the Rashba effect.[28−32] This effect is most prominent in the presence of heavy atoms such as with Pb, where spin-orbit coupling (SOC) plays a large role, or in symmetry-broken systems such as those seen in hybrid perovskites where the organic cations break inversion symmetry to allow for dispersive H—X interactions with the inorganic part of the structure.[33]

Due to the geometry-dependent prominence of the Rashba effect, multiple avenues have been explored to tune its strength and effect on band edges, such as the application of electric fields, strain, pressure, and temperature modulation.[34−38] For

Received: April 2, 2022
Accepted: July 11, 2022
Published: July 20, 2022

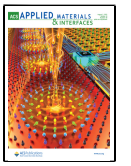

https://doi.org/10.1021/acsami.2c05842
ACS Appl. Mater. Interfaces 2022, 14, 34603−34611

example, Ju et al. noted the tunability of Rashba spin splitting under electric fields and strain, where $N^{III}X^{VI}$ systems exhibited tunable bandgaps insofar as the centrosymmetry of the lattice was broken.[39] Similarly, using pressure modulation to vary the strength of the Rashba effect, Wang et al. demonstrated an increase in the strength of direct transitions in an indirectly gapped perovskite system, which resulted in favorable performance for light absorption.[40] These previous studies highlight the important role geometric factors have on tuning Rashba splitting, which can be used to increase the efficiency of these low-dimensional materials in solar energy harvesting applications. Computational investigations provide a means by which the direct effect of these configurational changes on the electronic structure of such materials can be explored.

In this study, we used *ab initio* density functional theory (DFT) and Boltzmann transport equations (BTEs) to investigate the effect of strain on the electronic properties of two phases of stable 2DPKs derived from bulk $MAPbI_3$. Figure 1

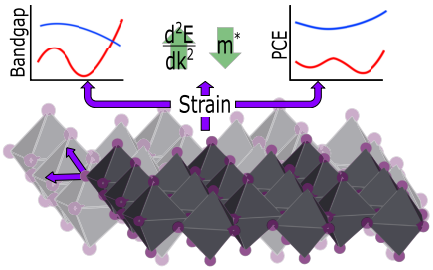

Figure 1. Schematic representation of the strain dependence of electronic properties such as power conversion efficiency, electronic bandgap, and effective mass exhibited in the 2D perovskite systems.

offers a schematic representation of the interplay between strain and electronic properties such as effective masses, power conversion efficiencies, and electronic bandgaps, as well as the fact that the PbI_6 octahedra (octahedral faces in gray, I atoms in purple) undergo a stretching in in-plane directions. We considered two different terminations of 2D forms of $MAPbI_3$, which have previously been studied computationally.[41] The first 2DPK phase, M1, was derived from the orthorhombic bulk structure and the second, M2, from the tetragonal structure. The M1 phase is surface terminated by $CH_3(CH_2)_3NH_3^+$ (BA), whereas the M2 phase is surface terminated by the $CH_3NH_3^+$ (MA) cations, giving chemical formulas of $(BA)_2(MA)_1Pb_2I_7$ (n = 2) and $(MA)_2PbI_4$ (n = 1) for the M1 and M2 phase, respectively. We applied a biaxial strain of −5, −2.5, 0, 2.5, and 5% to both phases along the in-plane directions (x, z for M1 and x, y for M2) to investigate the impact of structural changes on the optoelectronic and thermoelectric performance of the materials. Our results reveal the influence of strain on the Rashba effect, power conversion efficiency, and charge carrier dynamics governing transport properties of these 2DPKs. This study provides insight into the processes driving efficient solar energy harvesting in these materials.

RESULTS AND DISCUSSION

Structural Properties. Strain induces a variety of structural changes in halide perovskites including symmetry-altering phase transitions and local distortions in the lattice.[42,43] It leads to alterations of bond lengths and bond angles, which ultimately impact the orbital overlaps causing modifications in the electronic structure.[44] Upon compression of the unit cells, we find that in-plane Pb−I bond lengths tend to decrease, and out-of-plane bond lengths increase. This is expected as the unit cell is squeezed along the in-plane degrees of freedom, leading to extension of the out-of-plane bond lengths. At equilibrium, average Pb-I lengths are 3.22 and 3.21 Å in the M1 and M2 phases, respectively, which are in good agreement with the experimental results.[45] Our simulations demonstrate an inverted dependence of I−Pb−I bond angles on the strain between the M1 and M2 phases. In the M1 phase, the bond angle decreases with compression of the unit cell, whereas in the M2 phase, the bond angle increases with the same compression. These bond angle dependences directly correlate with the magnitude of the bandgap across the tested strains in the two phases, offering a geometrically tunable parameter for tailoring the bandgap. Liu et al. proposed that under consideration of Pb-I-Pb bond angles and bond lengths, the increased wave function overlap between Pb and I atoms leads to a narrowed bandgap.[44] However, our results show no such trend regarding the bond distances, but rather that conformal changes appear to have the largest effect on the bandgap of the materials.

Electronic Structure. Bond length and angle alterations change the band dispersion in the materials, which thereby modifies the bandgaps. The influence of strain on the electronic band structure for the M1 phase and the M2 phase is shown in Figure 2. For all strains in the M1 phase, the electronic bandgap is between 2.00 and 2.55 eV when excluding SOC and between 1.55 and 1.94 eV when including SOC. In both scenarios, the bandgap exhibits a sharp decrease between −2.5 and −5% strain. The bandgap fluctuates less than 50 meV between −2.5 and 5% strain. The large fluctuation in the bandgap between −5 and −2.5% strain is attributed to the changing placement of the valence band maximum (VBM) and the conduction band minimum (CBM). Upon inclusion of SOC, the CBM shifts from the ***T*-*U*** path to be very near the ***X*** point of the Brillouin zone (BZ), and the VBM shifts from the **Γ**-***X*** path to the ***S*-*R*** path. In calculations where SOC is not included, only the CBM shifts from the ***T*** point to the ***S*** point, while the VBM remains along the ***S*-*R*** path, in accordance with the SOC calculations. These qualitative differences highlight the importance of SOC for an accurate description of the band structure due to relativistic effects in the core of the heavy Pb atoms. Rashba splitting is observed along the ***U*-*S*-*R*and Γ-*X*-*Y*** directions, as can be seen in Figure 2a, and full band structures for calculations both with and without SOC for the M1 phase can be found in Figures S11 and S12.

For all strains in the M2 phase, electronic bandgaps range between 2.29 and 2.47 eV when excluding SOC, and between 1.44 and 1.58 eV when including SOC (Figure 2b). Fluctuations are at most 10 meV between −5 and 2.5% strain in SOC calculations, with a significant drop of 140 meV between 2.5 and 5% strain. Similarly, without consideration of SOC, the bandgap is lowest at 5% strain; however, fluctuations are much more significant across the tested values. In the SOC calculations, band edges always remain within the ***Y*-*Z*-*T*** path, with the CBM changing between the ***Y*-*Z*** and ***Z*-*T*** paths depending on the strain. In the absence of SOC, we often find degeneracy between the ***Z*** and **Γ** points, which is to be expected as they differ in the BZ by a wavevector in the aperiodic direction. Rashba splitting is observed along the *Y*-direction (present along the ***Y*-*Z*-*T*** path, but absent along **Γ**-***X***) in the M2 phase, as can be seen qualitatively in Figure 2b. The observed Rashba effect in both phases of 2DPK is strongly dependent on the number of inorganic layers and surface termination.[12,29] Electronic

https://doi.org/10.1021/acsami.2c05842
ACS Appl. Mater. Interfaces 2022, 14, 34603−34611

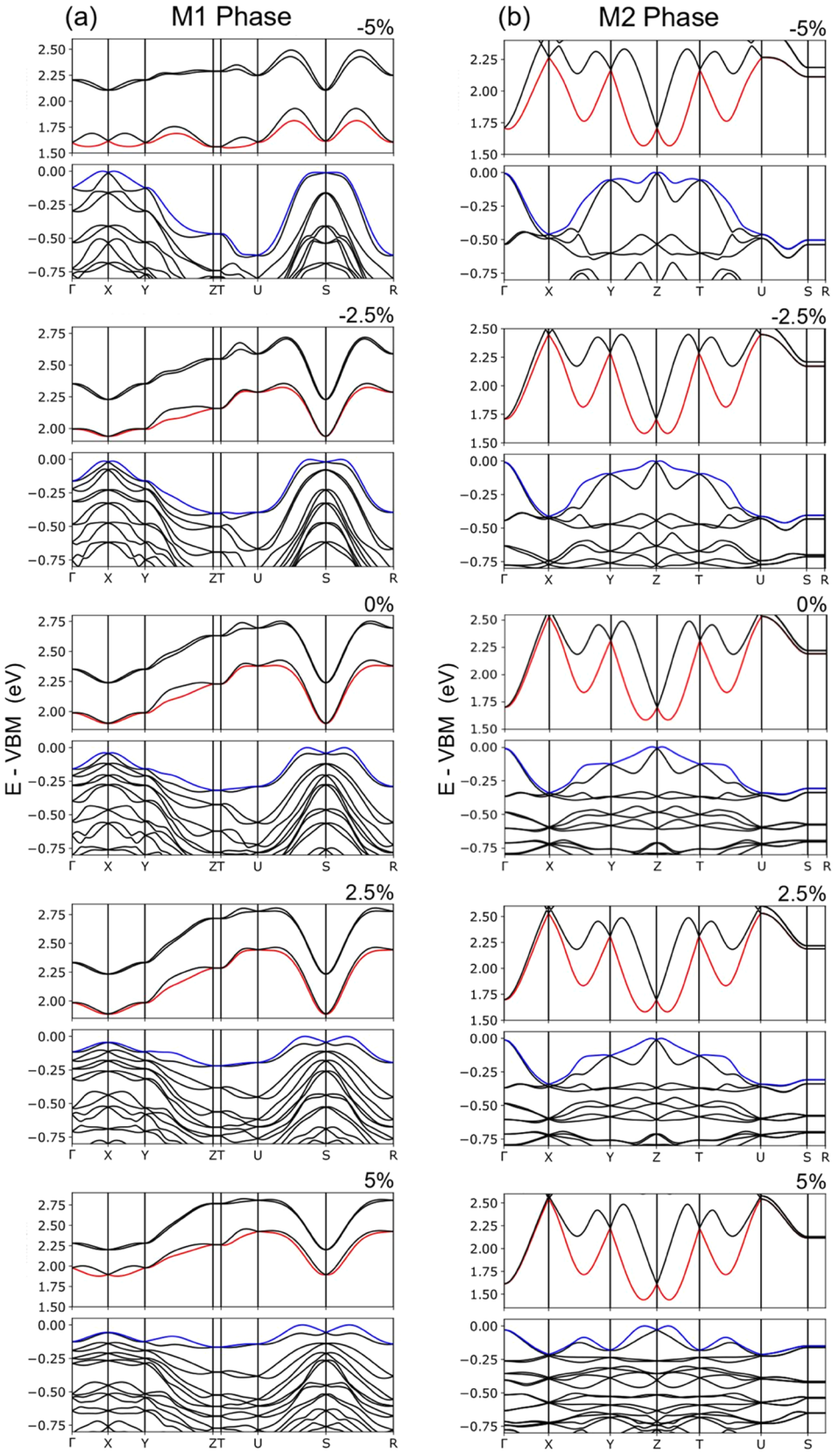

Figure 2. Band structures for the M1 phase with inclusion of spin-orbit coupling at −5, −2.5, 0, 2.5, and 5% strain for the (a) M1 Phase and (b) M2 phase. For clarity, the energy bands containing valence band maxima and conduction band minima are in blue and red, respectively.

structure calculations indicate that over all strains, the M1 and M2 phases have indirect bandgaps. Full electronic band structures with and without SOC for the M2 phase can be found in Figures S13 and S14.

https://doi.org/10.1021/acsami.2c05842
ACS Appl. Mater. Interfaces 2022, 14, 34603−34611

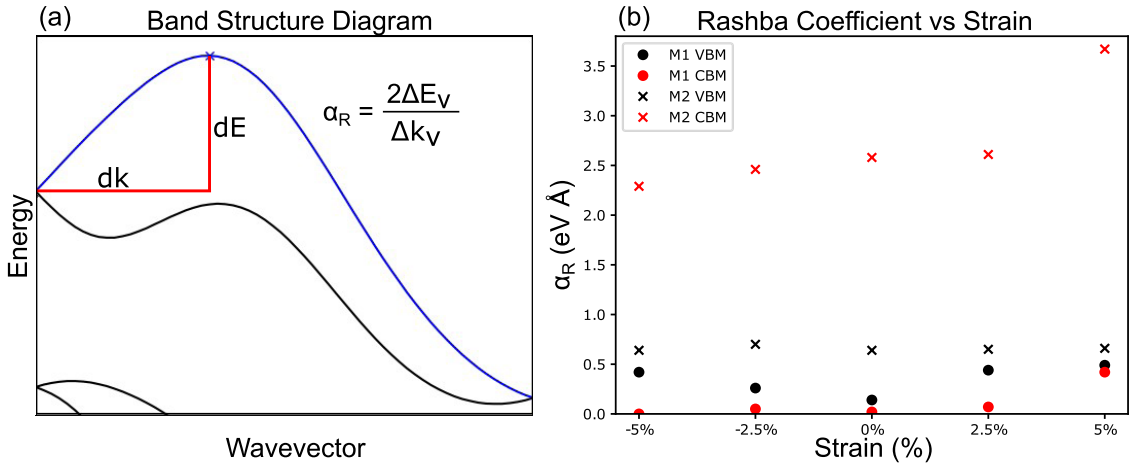

Figure 3. (a) Graphical representation of the quantities used for computation of eq 1, and (b) Rashba coefficients for the M1 and M2 phases as a function of strain.

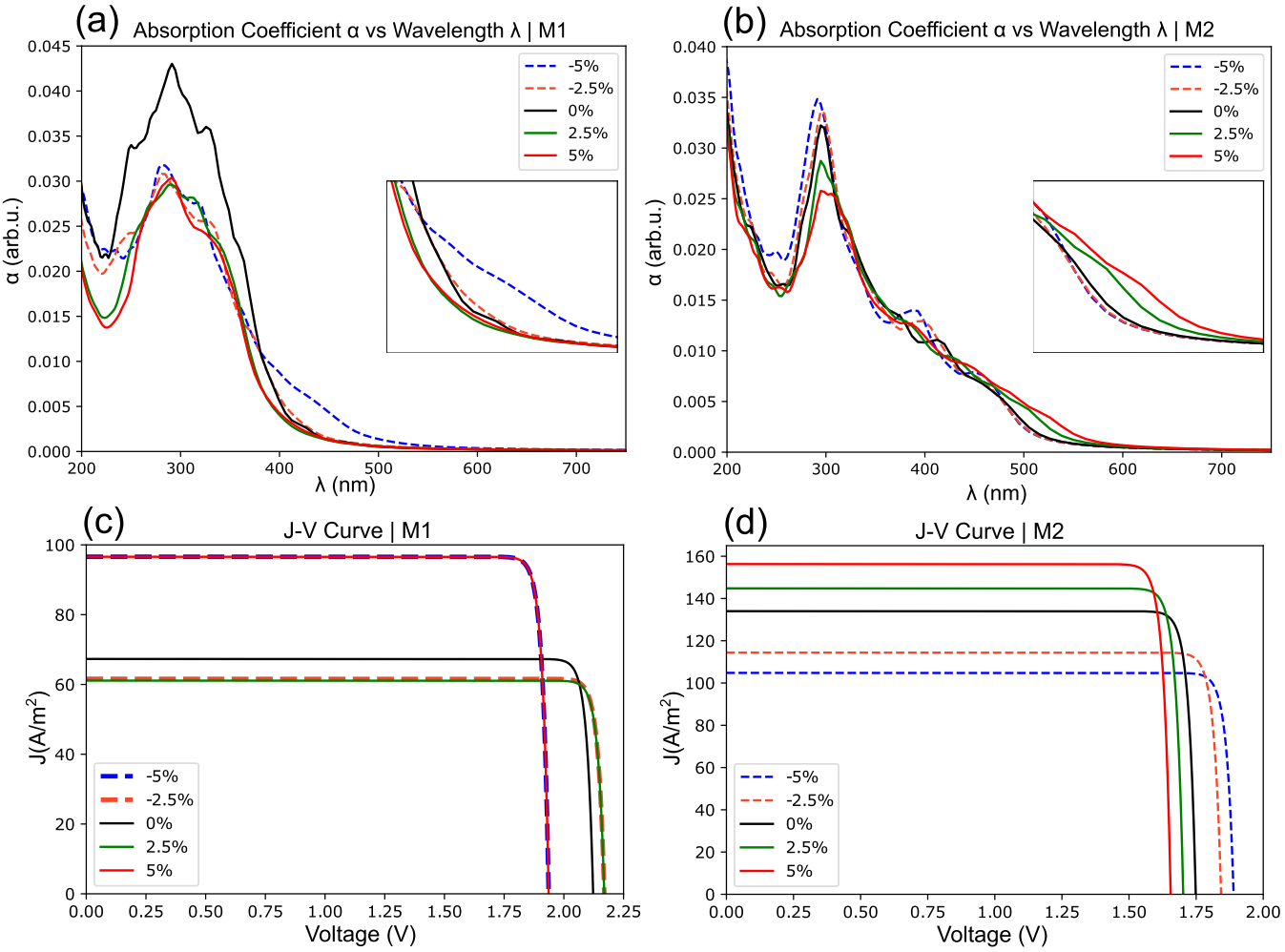

Figure 4. Optoelectrical properties for the 2D perovskites. (a, b) Absorption spectra for the M1 and M2 phases with insets from 360−500 and 460−600 nm, respectively. (c, d) Current voltage curves for the M1 and M2 phases.

To elucidate the influence of compression on the magnitude of Rashba splitting, the Rashba coefficients α_R were computed using the following equation:[46]

$$\alpha_R = 2\Delta E_v / \Delta k_v \quad (1)$$

where ΔE_v and Δk_v are the energy and wavevector difference, respectively, between the vertex of the Rashba split band and the band-crossing where the two-fold degeneracy has been lifted. A schematic diagram of the computation of the Rashba coefficient from the band structure is shown in Figure 3a. As shown in Figure 3b, the M1 phase has relatively lower Rashba coefficients

https://doi.org/10.1021/acsami.2c05842
ACS Appl. Mater. Interfaces 2022, 14, 34603−34611

compared to the M2 phase. The conduction band of M2 exhibits the highest Rashba coefficient, ranging between 2.29 and 3.67 eV Å, as shown in Figure 3b, consistent with the previous analysis of 2D-$MAPbI_3$ analogues.[12] A drastic increase from 2.61 to 3.67 eV Å is seen as strain increases from 2.5 to 5%. Although there is no well-defined structural parameter, which acts as an effective modulator of Rashba splitting in 2DPKs, indirect means of tuning the splitting mechanism have a significant effect on the carrier recombination process and provide valuable insights to improve the performance of solar cells. Both phases exhibit I(p)-Pb(p) transitions, as can be seen in the density of states (DOS) plots in Figures S1−S10. The upper part of the valence band is dominated by the I(p) states, with a small lower energy contribution from the 6(s) electrons of the Pb atoms, whereas the lower part of the conduction bands consists largely of Pb(p) states and, to a lesser degree, I(p) states. This p−p transition is well established in thin-film or 2D perovskite materials and is generally thought to be mediated by direct transition.[47,48]

Effect on Optoelectronic Properties. To investigate the influence of pressure-induced structural changes on the optical properties of the 2DPK, we examined optical absorption spectra for the M1 and M2 phases. The absorption spectra were obtained from the real and imaginary parts of the dielectric functions for the M1 (Figure 4a) and M2 phases (Figure 4b), for which more information can be found in the Computational Methods section. From the absorption spectra, Tauc plots were generated to determine optical bandgaps and short-circuit current densities J_{sc}, as listed in Table 1. The Tauc plot method

Table 1. Optical Properties of the M1 and M2 Phases as a Function of the Strain Applied to the Material

	strain (%)	E_{opt} (eV)	J_{sc} (A m^{-2})	V_{oc} (V)	FF (%)	PCE (%)
M1	−5	2.254	96.6	1.94	93.0	17.4
	−2.50	2.504	61.1	2.17	93.6	12.5
	0	2.454	67.3	2.12	93.5	13.4
	2.50	2.504	61.1	2.17	93.6	12.5
	5	2.254	96.6	1.94	93.0	17.4
M2	−5	2.204	104.8	1.89	92.8	18.4
	−2.50	2.154	114.4	1.84	92.7	19.5
	0	2.053	134.0	1.75	92.4	21.6
	2.50	2.003	144.8	1.7	92.2	22.7
	5	1.953	156.3	1.65	92.1	23.8

for optical bandgaps consists of plotting $(\alpha h\nu)^{1/r}$ (where $r = 2$ for indirect transitions) on the vertical axis against energy on the horizontal axis. The onset of the linear regime is then extrapolated to the abscissa, yielding the optical bandgap.[49] As shown in Figure 4a,b, in all absorption spectra, there is an initial gradual onset followed by a sharp peak at slightly higher energies. This two-step absorption process has been discussed previously in the context of perovskites as further supporting an indirect bandgap.[41,50] Furthermore, the inset of Figure 4a,b depicts that the gradual increase tends to occur around the DFT gap, while the sharp increase occurs beyond it, as direct transitions become energetically available. This is attributed to the fact that these lower lying excitations must be phonon-assisted due to the crystal momentum mismatch between the initial and final state of the electron. It is worth noting that despite the many-body nature of the phenomena responsible for the difference in absorption amplitudes between direct and indirect transitions, the single particle picture offered by the Kohn−Sham DFT has been shown to qualitatively explain this scenario in similar perovskite structures.[51] Quantitative assessment of the consequences of these phenomena on properties such as exciton lifetime requires additional treatment at the many-body level, which is beyond the scope of this work.[52] Regardless, the two-step onset of the absorption spectra, together with the linear regime found in the $r = 2$ Tauc plot, further supports determination from the electronic band structure that these minimum energy transitions are, in fact, indirect.

Using the optical bandgap, the short-circuit current density J_{sc} is computed using the following expression:[53]

$$J_{sc} = e\int_{E_{opt}}^{\infty} \frac{S(E)}{E} dE \tag{2}$$

where E_{opt} is the optical bandgap, $S(E)$ is the incident power on the Earth per unit area in accordance with the AM1.5G spectrum, and E is the incident photon energy. Using J_{sc}, current density as a function of voltage is obtained for computation of the open circuit voltage V_{oc} using the following equation:[41]

$$J(V) = J_{sc} - J_0(e^{eV/k_bT} - 1) \tag{3}$$

with V, T, and k_b representing the voltage, temperature (300 K in all calculations), and the Boltzmann constant, respectively. J_0 is obtained using the blackbody radiation spectra with the same equation as J_{sc}. V_{oc} is obtained as the x-intercept of the $J-V$ curve and is necessary for the assessment of the PCE of the perovskites. Figure 4c (Figure 4d) shows that V_{oc} represents the M1 (M2) phase. The PCE is assessed through the short-circuit current density J_{sc}, open circuit voltage V_{oc}, and the fill factor (FF) from the following equation:[54]

$$\text{PCE} = \frac{V_{oc}J_{sc}\text{FF}}{P_{in}} \tag{4}$$

where P_{in} is the incident power per unit area, taken to be 1 kW m^{-2} in accordance with the AM1.5G spectrum, and FF is computed as $\text{FF} = \frac{\vartheta_{oc} - \ln(\vartheta_{oc} + 0.72)}{\vartheta_{oc} + 1}$, using $\vartheta_{oc} = \frac{qV_{oc}}{k_bT}$, where q, k_b, and T are the elementary charge, Boltzmann constant, and temperature, respectively.

We find PCE in the M1 phase to have no clear dependence on the strain of the material; however in the M2 phase, there is a clear monotonic increase as the material is allowed to expand. It is worth noting that the PCEs presented in Table 1 are computed using quantities derived from DFT calculations, namely J_{sc}, which is determined by the optical bandgap. This means that due to DFT's well-established bandgap underestimation, optoelectronic quantities here should be considered relative to one another across the phases and strains, for which differences in the bandgap prove to be much more reliable, as opposed to the absolute value for direct comparison with the experiment.[55] Given this, our calculations clearly indicate that applications employing the M2 phase as a light absorbing layer, where the structure undergoes expansion of the lattice due to an interfacial mismatch or externally applied strain, will result in high efficiency for solar energy harvesting.

Effect on Thermoelectric Properties. In addition to the optical absorption properties, probing thermoelectric (TE) properties under strain is important as they govern carrier mobility and transport timescales. We investigated the TE properties of the two perovskite phases through the BTE in the constant relaxation time approximation (RTA).[56] TE properties

https://doi.org/10.1021/acsami.2c05842
ACS Appl. Mater. Interfaces 2022, 14, 34603−34611

Table 2. Charge Carrier Effective Masses, Mobilities, Relaxation Times, and Deformation Potentials as a Function of Strain and Crystallographic Axis for the M1 Phase

strain (%)	direction	m_e^* (m_e)	m_h^* (m_e)	E_{1VBM}	E_{1CBM}	μ_e (10^3cm^2/V s)	μ_h (10^3cm^2/V s)	τ_e (fs)	τ_h (fs)
−5.0	x	0.87	0.13	6.39	3.39	0.07	0.81	32.5	60.8
	z	0.21	0.17	8.35	5.38	0.29	0.20	35.3	18.7
−2.5	x	0.16	0.14	5.73	3.52	1.71	0.83	16.0	68.8
	z	0.08	0.15	7.13	10.63	0.54	0.32	24.4	28.0
0.0	x	0.16	0.17	4.89	3.38	2.01	0.86	18.1	81.5
	z	0.06	0.19	6.12	9.75	1.02	0.28	36.5	30.4
2.5	x	0.16	0.26	3.85	3.16	2.24	0.58	20.4	84.9
	z	0.07	0.23	5.43	9.01	1.09	0.24	40.8	31.7
5.0	x	0.18	0.37	3.9	3.24	1.71	0.27	17.4	93.4
	z	0.03	0.33	4.77	8.28	4.85	0.15	57.7	28.5

Table 3. Charge Carrier Effective Masses, Mobilities, Relaxation Times, and Deformation Potentials as a Function of Strain and Crystallographic Axis for the M2 Phase

strain (%)	direction	m_e^* (m_e)	m_h^* (m_e)	E_{1VBM}	E_{1CBM}	μ_e (10^3cm^2/V s)	μ_h (10^3cm^2/V s)	τ_e (fs)	τ_h (fs)
−5.0	x	0.08	0.07	7.64	7.25	1.18	1.29	50.3	50.0
	y	0.04	0.05	11.22	7.71	3.02	1.41	75.3	35.3
−2.5	x	0.09	0.08	6.94	6.87	0.82	1.06	44.2	49.8
	y	0.06	0.06	9.71	7.08	2.23	0.94	70.6	33.3
0.0	x	0.09	0.10	6.05	6.35	1.05	1.04	54.1	56.6
	y	0.05	0.08	7.98	6.49	3.04	0.84	89.7	38.3
2.5	x	0.11	0.12	5.21	5.46	0.91	0.96	58.7	63.2
	y	0.04	0.16	6.44	5.73	5.60	0.32	138.0	29.3
5.0	x	0.09	0.16	4.52	4.77	1.69	0.67	91.5	60.6
	y	0.04	0.32	5.34	5.16	8.27	0.12	186.2	21.2

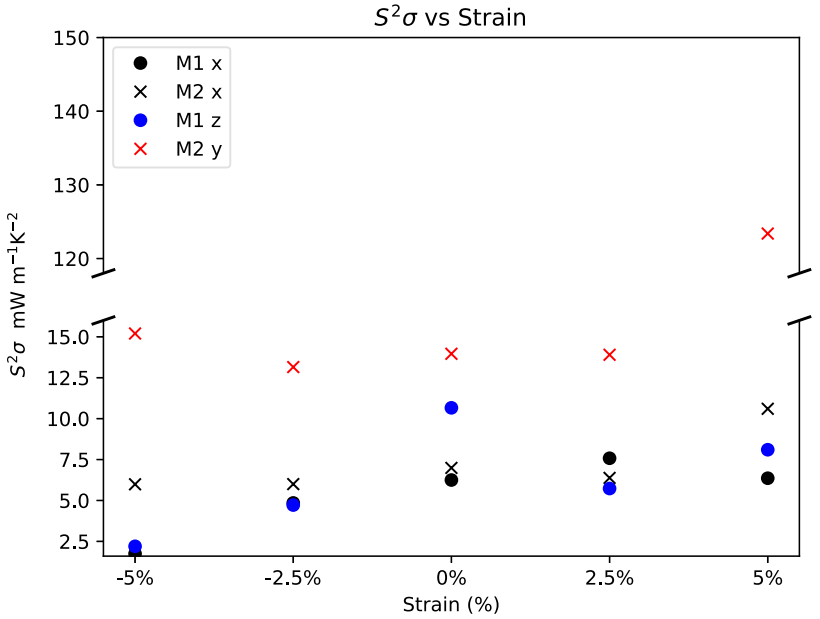

Figure 5. Peak thermoelectric power factor $S^2\sigma$ as a function of the applied strain.

were assessed using the Boltzwann module of the Wannier90 code. Details are described in the Computational Methods section. The carrier relaxation times (τ) as a function of strain were computed from first principles calculations using the relation $\tau = \frac{\mu m^*}{e}$, where μ, m^*, and e are the carrier mobility, the effective mass of charge carriers, and the charge of the electron, respectively. We employed the commonly used formulation for charge carrier mobility given as follows:[57,58]

$$\mu = \frac{2e\hbar^3 C^{2D}}{3k_b T(m^*)^2 E_1^2} \quad (5)$$

where C^{2D} refers to the in-plane stiffness constant and E_1 is the deformation potential of the relevant band edge. Details regarding calculation of these quantities can be found in the Computational Methods section. Table 2 (Table 3) contains all of the computed strain-dependent quantities for the M1 (M2) phase. In-plane stiffness constants were computed at 0% strain as the equilibrium cell parameters are required to obtain a

https://doi.org/10.1021/acsami.2c05842
ACS Appl. Mater. Interfaces 2022, 14, 34603−34611

parabolic fit to the energy−strain curve. C_x^{2D} and C_z^{2D} were 40.4 and 26.9 N m^{-1}, respectively, for the M1 phase, while C_x^{2D} and C_y^{2D} were 24.6 and 24.3 N m^{-1}, respectively, for the M2 phase. Our calculations indicate that the M2 phase is less rigid and can tolerate larger strain in application. Computed relaxation times in the subpicosecond range are found smaller than those in bulk perovskites but in line with the previous work on hybrid 2DPKs.[41,59] Similarly, computed values for the carrier mobilities are in line with previous computational studies on 2DPKs.[60,61] We attribute high carrier mobilities to the low effective masses, especially along the *z*-direction in the M1 phase, where large stiffness constants also aid in driving up mobility. Mobility of electrons in both the M1 and M2 phases drastically increases with tensile strain (117 and 143% increase from equilibrium for the M1 and M2 phase, respectively). Similarly, hole mobility decreases with tensile strain, attributed mainly to the drastic increase in effective masses (from 0.11 and 0.09 m_e at equilibrium to 0.35 and 0.24 m_e at 5% strain in the M1 and M2 phases, respectively). Average quantities are discussed above; however, it is important to highlight the strongly anisotropic properties of both phases, an example of which can be seen in the significantly higher electron mobility along the *y*-direction of the M2 phase.

The anisotropic nature of the TE properties is further borne out by the Seebeck coefficient (S), electrical conductivity (σ), and thermoelectric power factor (TPF) ($S^2\sigma$) of the materials. Figure 5 shows that the peak TPF value between a chemical potential of −2 and 2 eV as a function of strain for the two phases along the in-plane directions. Full plots of the Seebeck coefficient, electrical conductivity, and TPF as a function of chemical potential for the two phases can be found in Figures S17−S26, for which all calculations are run at a temperature of 300 K. The M1 phase generally exhibits a higher TPF for transport along the z-direction when strongly anisotropic performance is found (Figures 5 and S17−S21) with no clear trend in preference for n-doped or p-doped configurations. However, as shown in Figures S17−S21, maximum values of the Seebeck coefficient vary significantly with chemical potential across the different strains. At −5% strain, the highest Seebeck coefficient (3 mV K^{-1}, similar across all structures) occurs near the middle of the bandgap, leading to the low thermoelectric performance of this material under compression. As shown in Figures S22−S26, favorable TE properties in the M2 phase are clearly biased toward n-doped configurations, similar to the structure's bulk counterpart.[62] Unlike in the case of M1, there is no such change in the interplay between chemical potential and peaks in the Seebeck coefficient; rather changes in electrical conductivity drive the variation in the TE performance. Our calculations show that the TE properties of the M2 phase are strongly anisotropic with the peak TPF corresponding to transport along the *y*-direction. The largest TPF found in the M2 phase corresponds to a chemical potential of 1.99 eV with a TPF of 123 mW m^{-1} K^{-2}. The peak TPF in the M1 phase increases from 1.8 to 10.6 mW m^{-1} K^{-1} from −5 to 5% strain, indicating better TE performance with tensile strain. Our results clearly indicate that the M2 phase exhibits favorable performance as a thermoelectric, offering high efficiency for implementation as a mixed PV−TE material.

CONCLUSIONS

In summary, we present a systematic study of the influence of compressive and tensile strain on the electronic structure, optical properties, and thermoelectric properties of two stable phases of hybrid lead−iodide 2DPKs. Modulation in the electronic bandgaps results largely from conformal changes in the perovskite, whereby an increase in the I-Pb-I angle is directly correlated with a widening of the gap. This offers a tunable parameter with predictable outcomes on the electronic structure. Rashba splitting is found to be most prominent at the conduction band edge of the M2 phase at 5% strain, yielding a Rashba coefficient of 3.67 eV Å. The presence of strong Rashba spin splitting is particularly relevant for solar energy harvesting as it can be exploited to extend exciton lifetimes. The PCE of the M2 phase is found to be 23.8 at 5% tensile strain, the highest of all tested strains across both structures in the present study. Strongly anisotropic thermoelectric properties are revealed again, for which the M2 phase offers better performance, suggesting potentially efficient hybrid PV−TE applications. These strain-dependent properties offer valuable insights for applications in solar energy harvesting, and aid in understanding the role that conformal changes and organic cation orientation play in modulating the corresponding electronic structures.

COMPUTATIONAL METHODS

All DFT calculations were run using the Quantum Espresso package.[63] Fully relativistic norm-conserving pseudopotentials were used in all calculations.[64] Wave function and electronic density cutoffs were measured at 100 and 400 Ry, respectively. Variable cell geometry optimization calculations were used to determine the cell parameters to generate the various strained unit cells. After the generation of the unit cells from −5 to 5% strain, fixed cell optimizations were run. Geometry optimizations were carried out using the Broyden-Fletcher-Goldfarb-Shanno (BFGS) algorithm with a force convergence of 1e-3 Ha/Bohr and an electronic convergence of 1e-8 Ry on an 8 × 1 × 8 (8 × 8 × 1) grid for the M1 (M2) phase. A subsequent nonself-consistent calculation was run on a denser 12 × 12 × 1 (12 × 1 × 12) grid prior to computation of the density of states and electronic band structure. Band structure calculations were run with 300 k-points evenly spaced along the **ΓXYZTUSR** high symmetry path. Dielectric properties for optoelectronic computations were calculated at the random phase approximation (RPA) level on a 10 × 10 × 10 grid in accordance with the guidance of Quantum Espresso's epsilon.x package. Effective masses were computed in the parabolic band approximation, deformation potentials were computed using deformation potential theory, and stiffness constants were computed in accordance with computational literature analyzing 2D materials.[54] Calculation of thermoelectric properties using the Boltzmann transport equation in the constant relaxation time approximation was performed through Wannier90's BoltzWann module.[65,66] For Wannierization, 16 bands and 14 Wannier functions were used corresponding to nine valence bands and five conduction bands. All Boltzwann calculations followed Wannierizations, which were well converged with respect to the DFT band structure.

ASSOCIATED CONTENT

Supporting Information

The Supporting Information is available free of charge at https://pubs.acs.org/doi/10.1021/acsami.2c05842.

Plots of projected density of states, band structures, optoelectronic properties, thermoelectric properties, and fractional coordinates for the M1 and M2 phases of the 2DPK (PDF)

AUTHOR INFORMATION

Corresponding Author

Dhara J. Trivedi − *Department of Physics, Clarkson University, Potsdam, New York 13699, United States;* orcid.org/0000-0002-8151-3929; Email: dtrivedi@clarkson.edu

https://doi.org/10.1021/acsami.2c05842
ACS Appl. Mater. Interfaces 2022, 14, 34603−34611

Authors

Robert Stanton − *Department of Physics, Clarkson University, Potsdam, New York 13699, United States;* orcid.org/0000-0002-4989-6958

Sanjeev K. Gupta − *Department of Physics, St. Xavier's College, Ahmedabad 380009 Gujarat, India;* orcid.org/0000-0002-3060-2104

Complete contact information is available at: https://pubs.acs.org/10.1021/acsami.2c05842

Notes

The authors declare no competing financial interest.

■ ACKNOWLEDGMENTS

The authors (R.S. and D.J.T.) gratefully acknowledge support from the U.S. National Science Foundation (ECCS-2138728) and Clarkson University Faculty Start-up Fund. The computational work was supported in part by the Extreme Science and Engineering Discovery Environment (XSEDE), which is supported by the National Science Foundation (Grant no. TG-CHE210004). We thank P. Chattopadhyay for valuable comments.

■ REFERENCES

(1) Kojima, A.; K, T.; Y, S.; T, M. Organometal Halide Perovskites as Visible-Light Sensitizers for Photovoltaic Cells. *J. Am. Chem. Soc.* **2009**, *131*, 6050−6051.

(2) Park, N. G. Research Direction toward Scalable, Stable, and High Efficiency Perovskite Solar Cells. *Adv. Energy Mater.* **2020**, *10*, No. 1903106.

(3) Gharibzadeh, S.; Hossain, I. M.; Fassl, P.; Nejand, B. A.; Abzieher, T.; Schultes, M.; Ahlswede, E.; Jackson, P.; Powalla, M.; Schäfer, S.; Rienäcker, M.; Wietler, T.; Peibst, R.; Lemmer, U.; Richards, B. S.; Paetzold, U. W. 2D/3D Heterostructure for Semitransparent Perovskite Solar Cells with Engineered Bandgap Enables Efficiencies Exceeding 25% in Four-Terminal Tandems with Silicon and CIGS. *Adv. Funct. Mater.* **2020**, *30*, No. 1909919.

(4) Ma, C.; Park, N. G. A Realistic Methodology for 30% Efficient Perovskite Solar Cells. *Chem* **2020**, *6*, 1254−1264.

(5) Charles, B.; Dillon, J.; Weber, O. J.; Islam, M. S.; Weller, M. T. Understanding the Stability of Mixed A-Cation Lead Iodide Perovskites. *J. Mater. Chem. A* **2017**, *5*, 22495−22499.

(6) Yılmaz, B.; Odabaşı, Ç.; Yıldırım, R. Efficiency and Stability Analysis of 2D/3D Perovskite Solar Cells Using Machine Learning. *Energy Technol.* **2022**, *10*, No. 2100948.

(7) Li, W.; She, Y.; Vasenko, A. S.; Prezhdo, O. V. Ab Initio Nonadiabatic Molecular Dynamics of Charge Carriers in Metal Halide Perovskites. *Nanoscale* **2021**, *13*, 10239−10265.

(8) Wang, Y.; Pedesseau, L.; Katan, C.; Even, J.; Prezhdo, O. V.; Tretiak, S.; Ghosh, D.; Neukirch, A. J. Nonadiabatic Molecular Dynamics Analysis of Hybrid Dion-Jacobson 2D Leads Iodide Perovskites. *Appl. Phys. Lett.* **2021**, *119*, No. 201102.

(9) Wang, Y.; Fang, W. H.; Long, R.; Prezhdo, O. V. Symmetry Breaking at MAPbI 3 Perovskite Grain Boundaries Suppresses Charge Recombination: Time-Domain Ab Initio Analysis. *J. Phys. Chem. Lett.* **2019**, *10*, 1617−1623.

(10) Li, W.; Zhou, L.; Prezhdo, O. V.; Akimov, A. V. Spin-Orbit Interactions Greatly Accelerate Nonradiative Dynamics in Lead Halide Perovskites. *ACS Energy Lett.* **2018**, *3*, 2159−2166.

(11) Ricci, F.; Marougail, V.; Varnavski, O.; Wu, Y.; Padgaonkar, S.; Irgen-Gioro, S.; Weiss, E. A.; Goodson, T. Enhanced Exciton Quantum Coherence in Single CsPbBr3 Perovskite Quantum Dots Using Femtosecond Two-Photon Near-Field Scanning Optical Microscopy. *ACS Nano* **2021**, *15*, 12955−12965.

(12) Yin, J.; Maity, P.; Xu, L.; El-Zohry, A. M.; Li, H.; Bakr, O. M.; Brédas, J. L.; Mohammed, O. F. Layer-Dependent Rashba Band Splitting in 2D Hybrid Perovskites. *Chem. Mater.* **2018**, *30*, 8538−8545.

(13) Li, Y.; Wang, T.; Wu, M.; Cao, T.; Chen, Y.; Sankar, R.; Ulaganathan, R. K.; Chou, F.; Wetzel, C.; Xu, C. Y.; Louie, S. G.; Shi, S. F. Ultrasensitive Tunability of the Direct Bandgap of 2D InSe Flakes via Strain Engineering. *2D Mater.* **2018**, *5*, No. 021002.

(14) Aslan, B.; Yule, C.; Yu, Y.; Lee, Y. J.; Heinz, T. F.; Cao, L.; Brongersma, M. L. Excitons in Strained and Suspended Monolayer WSe2. *2D Mater.* **2022**, *9*, No. 015002.

(15) Luan, X.; Zheng, Z.; Wang, Z.; Gao, Y.; Zhao, S.; Xue, Y.; Li, Y. Graphdiyne/CdSe Quantum Dot Heterostructure for Efficient Photoelectrochemical Water Oxidation. *2D Mater.* **2021**, *8*, No. 044017.

(16) Zhang, L.; Liang, W. How the Structures and Properties of Two-Dimensional Layered Perovskites MAPbI3 and CsPbI3 Vary with the Number of Layers. *J. Phys. Chem. Lett.* **2017**, *8*, 1517−1523.

(17) Liu, J.; Xue, Y.; Wang, Z.; Xu, Z. Q.; Zheng, C.; Weber, B.; Song, J.; Wang, Y.; Lu, Y.; Zhang, Y.; Bao, Q. Two-Dimensional CH3NH3PbI3 Perovskite: Synthesis and Optoelectronic Application. *ACS Nano* **2016**, *10*, 3536−3542.

(18) Zhang, L.; Sun, C.; He, T.; Jiang, Y.; Wei, J.; Huang, Y.; Yuan, M. High-Performance Quasi-2D Perovskite Light-Emitting Diodes: From Materials to Devices. *Light Sci.: Appl.* **2021**, *10*, No. 61.

(19) Hsu, S.-N.; Zhao, W.; Gao, Y.; Akriti; Segovia, M.; Xu, X.; Boudouris, B. W.; Dou, L. Thermoelectric Performance of Lead-Free Two-Dimensional Halide Perovskites Featuring Conjugated Ligands. *Nano Lett.* **2021**, *21*, 7839−7844.

(20) Blancon, J. C.; Even, J.; Stoumpos, C. C.; Kanatzidis, M. G.; Mohite, A. D. Semiconductor Physics of Organic−Inorganic 2D Halide Perovskites. *Nat. Nanotechnol.* **2020**, *15*, 969−985.

(21) Zhang, F.; Kim, D. H.; Zhu, K. 3D/2D Multidimensional Perovskites: Balance of High Performance and Stability for Perovskite Solar Cells. *Curr. Opin. Electrochem.* **2018**, *11*, 105−113.

(22) Saikia, N.; Seel, M.; Pandey, R. Stability and Electronic Properties of 2D Nanomaterials Conjugated with Pyrazinamide Chemotherapeutic: A First-Principles Cluster Study. *J. Phys. Chem. C* **2016**, *120*, 20323−20332.

(23) Kim, J. Y.; Lee, J. W.; Jung, H. S.; Shin, H.; Park, N. G. High-Efficiency Perovskite Solar Cells. *Chem. Rev.* **2020**, *120*, 7867−7918.

(24) Wang, X.; Wang, Y.; Zhang, T.; Liu, X.; Zhao, Y. Steric Mixed-Cation 2D Perovskite as a Methylammonium Locker to Stabilize MAPbI3. *Angew. Chem.* **2020**, *132*, 1485−1489.

(25) Cao, F.; Wang, M.; Li, L. Graded Energy Band Engineering for Efficient Perovskite Solar Cells. *Nano Sel.* **2020**, *1*, 152−168.

(26) Fang, C.; Wang, H.; Li, D. Recent Progress in Two-Dimensional Ruddlesden−Popper Perovskite Based Heterostructures. *2D Mater.* **2021**, *8*, No. 022006.

(27) Quan, L. N.; Zhao, Y.; García De Arquer, F. P.; Sabatini, R.; Walters, G.; Voznyy, O.; Comin, R.; Li, Y.; Fan, J. Z.; Tan, H.; Pan, J.; Yuan, M.; Bakr, O. M.; Lu, Z.; Kim, D. H.; Sargent, E. H. Tailoring the Energy Landscape in Quasi-2D Halide Perovskites Enables Efficient Green-Light Emission. *Nano Lett.* **2017**, *17*, 3701−3709.

(28) Huang, G.; Rassel, S.; Qu, J.; Xu, S.; Wang, C.; Ban, D. Manipulation of Spin Splitting in Two-Dimensional Lead Bromide Perovskite Rashba Piezoelectrics. *ACS Appl. Electron. Mater.* **2021**, *3*, 285−291.

(29) Pham, M. T.; Amerling, E.; Luong, H. M.; Pham, H. T.; Larsen, G. K.; Whittaker-Brooks, L.; Nguyen, T. D. Origin of Rashba Spin-Orbit Coupling in 2D and 3D Lead Iodide Perovskites. *Sci. Rep.* **2020**, *10*, No. 4964.

(30) Zheng, F.; Tan, L. Z.; Liu, S.; Rappe, A. M. Rashba Spin-Orbit Coupling Enhanced Carrier Lifetime in CH3NH3PbI3. *Nano Lett.* **2015**, *15*, 7794−7800.

(31) Kim, K. Y.; Park, G.; Cho, J.; Kim, J.; Kim, J. S.; Jung, J.; Park, K.; You, C. Y.; Oh, I. H. Intrinsic Magnetic Order of Chemically Exfoliated 2D Ruddlesden−Popper Organic−Inorganic Halide Perovskite Ultrathin Films. *Small* **2020**, *16*, 1−12.

(32) Jana, M. K.; Song, R.; Liu, H.; Khanal, D. R.; Janke, S. M.; Zhao, R.; Liu, C.; Valy Vardeny, Z.; Blum, V.; Mitzi, D. B. Organic-to-

Inorganic Structural Chirality Transfer in a 2D Hybrid Perovskite and Impact on Rashba-Dresselhaus Spin-Orbit Coupling. *Nat. Commun.* **2020**, *11*, No. 4699.
(33) Frohna, K.; Deshpande, T.; Harter, J.; Peng, W.; Barker, B. A.; Neaton, J. B.; Louie, S. G.; Bakr, O. M.; Hsieh, D.; Bernardi, M. Inversion Symmetry and Bulk Rashba Effect in Methylammonium Lead Iodide Perovskite Single Crystals. *Nat. Commun.* **2018**, *9*, No. 1829.
(34) Gong, S. J.; Duan, C. G.; Zhu, Y.; Zhu, Z. Q.; Chu, J. H. Controlling Rashba Spin Splitting in Au(111) Surface States through Electric Field. *Phys. Rev. B* **2013**, *87*, 3−6.
(35) Eldridge, P. S.; Leyland, W. J. H.; Lagoudakis, P. G.; Karimov, O. Z.; Henini, M.; Taylor, D.; Phillips, R. T.; Harley, R. T. All-Optical Measurement of Rashba Coefficient in Quantum Wells. *Phys. Rev. B* **2008**, *77*, No. 125344.
(36) Yang, W.; Guan, Z.; Wang, H.; Li, J. Ideal Strength and Strain Engineering of the Rashba Effect in Two-Dimensional BiTeBr. *Phys. Chem. Chem. Phys.* **2021**, *23*, 6552−6560.
(37) Jaffe, A.; Lin, Y.; Karunadasa, H. I. Halide Perovskites under Pressure: Accessing New Properties through Lattice Compression. *ACS Energy Lett.* **2017**, *2*, 1549−1555.
(38) Zhu, L.; Wang, Z. L. Piezotronic Effect on Rashba Spin-Orbit Coupling Based on MAPbI3/ZnO Heterostructures. *Appl. Phys. Lett.* **2020**, *117*, No. 071601.
(39) Ju, W.; Wang, D.; Li, T.; Wang, H.; Zhou, Q.; Xu, Y.; Li, H.; Gong, S. Electric Field Control of Rashba Spin Splitting in 2D NIIIXVI (N = Ga, In; X = S, Se, Te) Monolayer. *J. Phys. Condens. Matter* **2020**, *32*, No. 175503.
(40) Wang, T.; Daiber, B.; Frost, J. M.; Mann, S. A.; Garnett, E. C.; Walsh, A.; Ehrler, B. Indirect to Direct Bandgap Transition in Methylammonium Lead Halide Perovskite. *Energy Environ. Sci.* **2017**, *10*, 509−515.
(41) Kagdada, H. L.; Gupta, S. K.; Sahoo, S.; Singh, D. K. Rashba Splitting in Two Dimensional Hybrid Perovskite Materials for High Efficient Solar and Heat Energy Harvesting. *J. Phys. Chem. Lett.* **2020**, *11*, 7679−7686.
(42) Wu, S. Q.; Cheng, S.; Lu, L.; Liu, M.; Jin, X. W.; Cheng, S. D.; Mi, S. B. B-Site Ordering and Strain-Induced Phase Transition in Double-Perovskite La2NiMnO6 Films. *Sci. Rep.* **2018**, *8*, No. 2516.
(43) Liu, D.; Luo, D.; Iqbal, A. N.; Orr, K. W. P.; Doherty, T. A. S.; Lu, Z. H.; Stranks, S. D.; Zhang, W. Strain Analysis and Engineering in Halide Perovskite Photovoltaics. *Nat. Mater.* **2021**, *20*, 1337−1346.
(44) Liu, G.; Gong, J.; Kong, L.; Schaller, R. D.; Hu, Q.; Liu, Z.; Yan, S.; Yang, W.; Stoumpos, C. C.; Kanatzidis, M. G.; Mao, H. kwang.; Xu, T. Isothermal Pressure-Derived Metastable States in 2D Hybrid Perovskites Showing Enduring Bandgap Narrowing. *Proc. Natl. Acad. Sci. U.S.A.* **2018**, *115*, 8076−8081.
(45) Mei, A.; Sheng, Y.; Ming, Y.; Hu, Y.; Rong, Y.; Zhang, W.; Luo, S.; Na, G.; Tian, C.; Hou, X.; Xiong, Y.; Zhang, Z.; Liu, S.; Uchida, S.; Kim, T. W.; Yuan, Y.; Zhang, L.; Zhou, Y.; Han, H. Stabilizing Perovskite Solar Cells to IEC61215:2016 Standards with over 9,000-h Operational Tracking. *Joule* **2020**, *4*, 2646−2660.
(46) Zhai, Y.; Baniya, S.; Zhang, C.; Li, J.; Haney, P.; Sheng, C. X.; Ehrenfreund, E.; Vardeny, Z. V. Giant Rashba Splitting in 2D Organic-Inorganic Halide Perovskites Measured by Transient Spectroscopies. *Sci. Adv.* **2017**, *3*, No. e1700704.
(47) Yin, W. J.; Shi, T.; Yan, Y. Unique Properties of Halide Perovskites as Possible Origins of the Superior Solar Cell Performance. *Adv. Mater.* **2014**, *26*, 4653−4658.
(48) Yin, W. J.; Shi, T.; Yan, Y. Superior Photovoltaic Properties of Lead Halide Perovskites: Insights from First-Principles Theory. *J. Phys. Chem. C* **2015**, *119*, 5253−5264.
(49) Makuła, P.; Pacia, M.; Macyk, W. How To Correctly Determine the Band Gap Energy of Modified Semiconductor Photocatalysts Based on UV-Vis Spectra. *J. Phys. Chem. Lett.* **2018**, *9*, 6814−6817.
(50) Deschler, F.; Price, M.; Pathak, S.; Klintberg, L. E.; Jarausch, D. D.; Higler, R.; Hüttner, S.; Leijtens, T.; Stranks, S. D.; Snaith, H. J.; Atatüre, M.; Phillips, R. T.; Friend, R. H. High Photoluminescence Efficiency and Optically Pumped Lasing in Solution-Processed Mixed Halide Perovskite Semiconductors. *J. Phys. Chem. Lett.* **2014**, *5*, 1421−1426.
(51) Motta, C.; El-Mellouhi, F.; Kais, S.; Tabet, N.; Alharbi, F.; Sanvito, S. Revealing the Role of Organic Cations in Hybrid Halide Perovskite CH3NH3PbI3. *Nat. Commun.* **2015**, *6*, No. 7026.
(52) Smith, B.; Shakiba, M.; Akimov, A. V. Crystal Symmetry and Static Electron Correlation Greatly Accelerate Nonradiative Dynamics in Lead Halide Perovskites. *J. Phys. Chem. Lett.* **2021**, *12*, 2444−2453.
(53) Nelson, J. *The Physics of Solar Cells*; Imperial College Press: London, U.K., 2003.
(54) Kumavat, S. R.; Sonvane, Y.; Singh, D.; Gupta, S. K. Two-Dimensional CH3NH3PbI3 with High Efficiency and Superior Carrier Mobility: A Theoretical Study. *J. Phys. Chem. C* **2019**, *123*, 5231−5239.
(55) Bagayoko, D. Understanding Density Functional Theory (DFT) and Completing It in Practice. *AIP Adv.* **2014**, *4*, No. 127104.
(56) Mermin, N. D. Lindhard Dielectric Function in the Relaxation-Time Approximation. *Phys. Rev. B* **1970**, *1*, 2362−2363.
(57) Cai, Y.; Zhang, G.; Zhang, Y. W. Polarity-Reversed Robust Carrier Mobility in Monolayer MoS2 Nanoribbons. *J. Am. Chem. Soc.* **2014**, *136*, 6269−6275.
(58) Sharma, V.; Kagdada, H. L.; Jha, P. K.; Śpiewak, P.; Kurzydłowski, K. J. Halogenation of SiGe Monolayers: Robust Changes in Electronic and Thermal Transport. *Phys. Chem. Chem. Phys.* **2019**, *21*, 19488−19498.
(59) Motta, C.; El-Mellouhi, F.; Sanvito, S. Charge Carrier Mobility in Hybrid Halide Perovskites. *Sci. Rep.* **2015**, *5*, No. 12746.
(60) Huang, K.; Lai, K.; Yan, C. L.; Zhang, W. B. Stability and Carrier Mobility of Organic-Inorganic Hybrid Perovskite CH3NH3PbI3 in Two-Dimensional Limit. *J. Chem. Phys.* **2017**, *147*, No. 164703.
(61) Du, J.; Shi, J. jie. 2D Ca3Sn2S7 Chalcogenide Perovskite: A Graphene-Like Semiconductor with Direct Bandgap 0.5 eV and Ultrahigh Carrier Mobility 6.7×10^4 cm^2 V^{-1} S^{-1}. *Adv. Mater.* **2019**, *31*, No. 1905643.
(62) Ali, I. O. A.; Joubert, D. P.; Suleiman, M. S. H. A Theoretical Investigation of Structural, Mechanical, Electronic and Thermoelectric Properties of Orthorhombic CH3NH3PbI3. *Eur. Phys. J. B* **2018**, *91*, No. 263.
(63) Giannozzi, P.; Baroni, S.; Bonini, N.; Calandra, M.; Car, R.; Cavazzoni, C.; Ceresoli, D.; Chiarotti, G. L.; Cococcioni, M.; Dabo, I.; Dal Corso, A.; De Gironcoli, S.; Fabris, S.; Fratesi, G.; Gebauer, R.; Gerstmann, U.; Gougoussis, C.; Kokalj, A.; Lazzeri, M.; Martin-Samos, L.; Marzari, N.; Mauri, F.; Mazzarello, R.; Paolini, S.; Pasquarello, A.; Paulatto, L.; Sbraccia, C.; Scandolo, S.; Sclauzero, G.; Seitsonen, A. P.; Smogunov, A.; Umari, P.; Wentzcovitch, R. M. QUANTUM ESPRESSO: A Modular and Open-Source Software Project for Quantum Simulations of Materials. *J. Phys. Condens. Matter* **2009**, *21*, No. 395502.
(64) Hamann, D. R. Optimized Norm-Conserving Vanderbilt Pseudopotentials. *Phys. Rev. B* **2013**, *88*, No. 085117.
(65) Mostofi, A. A.; Yates, J. R.; Pizzi, G.; Lee, Y. S.; Souza, I.; Vanderbilt, D.; Marzari, N. An Updated Version of Wannier90: A Tool for Obtaining Maximally-Localised Wannier Functions. *Comput. Phys. Commun.* **2014**, *185*, 2309−2310.
(66) Pizzi, G.; Volja, D.; Kozinsky, B.; Fornari, M.; Marzari, N. BoltzWann: A Code for the Evaluation of Thermoelectric and Electronic Transport Properties with a Maximally-Localized Wannier Functions Basis. *Comput. Phys. Commun.* **2014**, *185*, 422−429.

https://doi.org/10.1021/acsami.2c05842
ACS Appl. Mater. Interfaces 2022, 14, 34603−34611